ChemPubSoc Europe

DOI: 10.1002/chem.201800380

CHEMISTRY A European Journal Full Paper

Equatorial Fe^{IV} Ligation

Axial vs. Equatorial Ligand Rivalry in Controlling the Reactivity of Iron(IV)-Oxo Species: Single-State vs. Two-State Reactivity

Ravi Kumar[+],[a] Azaj Ansari[+],[b] and Gopalan Rajaraman*[a]

Abstract: High-valent iron-oxo species are known for their very high reactivity, and this aspect has been studied in detail over the years. The role of axial ligands in fine-tuning the reactivity of the iron(IV)-oxo species has been particularly well studied. The corresponding role of equatorial ligands, however, has rarely been explored, and is of prime importance in the development of non-heme chemistry. Here, we have undertaken detailed DFT calculations on $[(L^{NHC})Fe^{IV}(O)(CH_3CN)]^{2+}$ (**1**; L^{NHC} = 3,9,14,20-tetraaza-1,6,12,17-tetraazoniapenta-cyclohexacosane-1(23),4,6(26),10,12(25),15,17(24),21-octaene) in comparison to compound II of cytochrome P450 $[(porphyrin)Fe^{IV}(O)(SH)]^{-}$ (**2**) to probe this aspect. The electronic structures of **1** and **2** are found to vary significantly, implying a large variation in their reactivities. In particular, the strong equatorial ligand present in **1** significantly destabilizes the quintet states as compared to species **2**. To fully understand the reactivity pattern of these species, we have modelled the hydroxylation of methane by both **1** and **2**. Our calculations reveal that **1** reacts via a low-lying $S=1$ π pathway, and that the generally available $S=2$ σ pathway is not energetically accessible. In addition to having a significant barrier for C–H bond activation, the -OH rebound step is also computed to have a large barrier height, leading to a marked difference in reactivity between these two species. Of particular relevance here is the observation of pure triplet-state reactivity for **1**. We have also attempted to test the role of axial ligands in fine-tuning the reactivity of **1**, and our results demonstrate that, in contrast to heme systems, the axial ligands in **1** do not significantly influence the reactivity. This highlights the importance of designing equatorial ligands to fine-tune reactivity of high-valent iron(IV)-oxo species.

Introduction

High-valent iron-oxo species are key intermediates in the catalytic cycles of heme and non-heme iron enzymes that insert an oxygen atom from dioxygen into non-labile C–H bonds of aliphatic and aromatic hydrocarbons.[1] In heme iron enzymes such as cytochrome P450, iron(IV)-oxo cation radical porphyrin compound (cpd I) and iron(IV)-oxo porphyrin compound (cpd II) are suggested as the reactive intermediates.[2] Cpd I has biological significance and has been explored in detail over the years. Cpd II is also found to activate C–H bonds of alkanes.[2i,3] To better understand and tune their reactivities, several model complexes have been synthesized to mimic the reactivities of the metalloenzymes.[1,2c,4] Numerous efforts have been made to synthesize and characterize model heme and non-heme iron complexes.[1a,2] Their reactivities toward C–H bond activation have been studied both experimentally and theoretically. One possible way to fine-tune the reactivity is to alter the nature of the axial ligands. This has been proposed and studied in detail for cytochrome P450 enzymes. In cytochrome P450 and related model complexes,[2a,5] weaker axial ligands are found to decrease the reactivity of the species towards hydrogen atom transfer (HAT) reactions. For example, an imidazole axial ligand imparts lower reactivity than an -SH axial ligand.[2a,5]

Models reported to mimic non-heme enzymes are based on aminopyridine ligands, which offer weak to moderate ligand fields. Whereas the role of axial ligands in biomimetic non-heme iron(IV)-oxo models has been delineated,[6] how substantially stronger equatorial ligands alter the reactivity has not been established. This is an attractive idea and is now starting to be explored. Specifically, carbene-based organometallic catalysts have been synthesized and characterized.[7] These catalysts have also been found to promote C–H bond activation, epoxidation, and N–H insertion.[7,8] In this context, efforts have been made to fine-tune the equatorial ligands,[9] most notably the synthesis and reactivity studies of an iron(IV)-oxo complex bearing a macrocyclic tetracarbene ligand ($[(L^{NHC})Fe^{IV}(O)(CH_3CN)]^{2+}$ (**1**) where L^{NHC} = 3,9,14,20-tetraaza-1,6,12,17-tetraazoniapenta-cyclohexacosane-1(23),4,6(26),10,12(25),15,17(24),21-octaene).[10] In complex **1**, the carbene carbon atoms are found to coordinate at the equatorial positions, leading to a stable iron(IV)-oxo species.

[a] *R. Kumar,[+] Prof. Dr. G. Rajaraman*
Department of Chemistry, Indian Institute of Technology Bombay
Powai, Mumbai, 400076 (India)
E-mail: rajaraman@chem.iitb.ac.in

[b] *Dr. A. Ansari[+]*
Department of Chemistry, Central University of Haryana
Haryana, 123031 (India)

[+] *These authors contributed equally to this work.*

Supporting information and the ORCID number(s) for the author(s) of this article can be found under https://doi.org/10.1002/chem.201800380.

We have now undertaken a detailed theoretical study to address a number of intriguing issues: (i) why species **1** exhibits high stability compared to other reported iron(IV)-oxo species; (ii) the comparability of the electronic structures and reactivities of species **1** and **2**; and (iii) whether the axial ligand can be used to fine-tune the reactivity in **1** (Scheme 1).

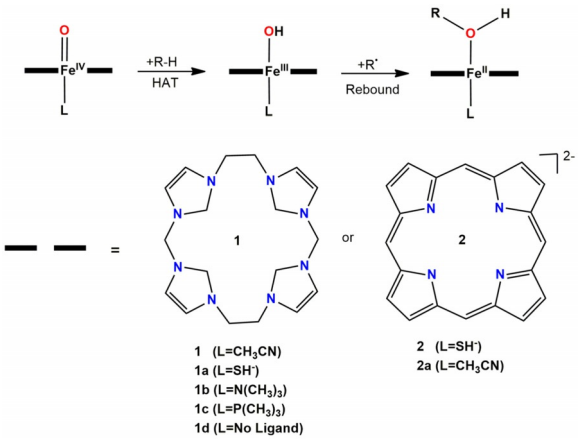

Scheme 1. The hydroxylation process by tetracarbene and cytochrome P450 cpd II iron(IV)-oxo reagents with variable axial ligands: **1** ($[(L^{NHC})Fe^{IV}(O)(CH_3CN)]^{2+}$), **1a** ($[(L^{NHC})Fe^{IV}(O)(SH)]^{+}$), **1b** ($[(L^{NHC})Fe^{IV}(O)(N(CH_3)_3)]^{2+}$), **1c** ($[(L^{NHC})Fe^{IV}(O)(N(CH_3)_3)]^{2+}$), **1d** ($[(L^{NHC})Fe^{IV}(O)]^{2+}$), **2** ([(porphyrin)$Fe^{IV}$(O)(SH)]$^{-}$), and **2a** ([(porphyrin)Fe^{IV}(O)(CH_3CN)]).

Computational details

In the present work, all calculations were performed using established procedures.[5b,11] Geometry optimization was carried out with Gaussian 09 software,[12] whereas all spectroscopic parameters were calculated with the ORCA 3.0 program package incorporating COSMO solvation effects.[13] Geometries were optimized using Grimme's dispersion-corrected unrestricted B3LYP functional (UB3LYP-D2).[14] We carried out optimizations and frequency calculations with the LANL2DZ double-ζ-quality basis set, with the Los Alamos effective core potential for Fe and a 6-31G basis set for C, H, O, N, P, and S,[15] and then performed single-point energy calculations using the TZVP[11e,16] basis set for all atoms. To ascertain the role of basis sets, geometry optimizations were also performed with the LANL2TZ basis set for Fe and the 6-31G* basis set for other atoms. The structural parameters and the computed energies were found to be only marginally altered by using this higher basis set (see Tables S5 and S6 in the Supporting Information). Frequency calculations were performed on the optimized structures to verify that they were minima on the potential-energy surface (PES) and also to obtain free-energy corrections. The quoted DFT energies are UB3LYP-D2/TZVP solvation energies including free-energy corrections, at 298.15 K unless otherwise mentioned. Since most of the species studied in this work have a charge of +2, gas-phase optimizations employing lower basis sets are prone to self-interaction errors (SIE). To avoid this issue, we also performed solvent-phase optimizations for selected species. However, only minor alterations in the values were noted, as indicated in Table S3 in the Supporting Information. The optimized geometries were further verified by animating frequency using Chemcraft software.[17] The solvation energies were computed at the UB3LYP-D2 level using the polarizable continuum model (PCM) with acetonitrile as solvent. Spin density visualizations were achieved using Chemcraft software.[18] All spectroscopic parameters were calculated by taking into account relativistic effects based on a zeroth-order regular approximation method (ZORA) as implemented in the ORCA suite.[19] Mössbauer isomer shifts (δ) were calculated on the basis of calibration constants reported by Römelt et al., and 0.16 barn was used for the calculation of quadrupole moments of ^{57}Fe nuclei.[20] We performed state-average complete active space self-consistent field (SA-CASSCF) calculations to compute the zero-field splitting (ZFS) parameters of **1**, wherein dynamic correlations were incorporated using second-order N-electron valence perturbation theory (NEVPT2). We employed the def2-TZVP basis set for these calculations. The active space for CASSCF calculations comprises five Fe^{IV}-based orbitals with four electrons therein (d^4 system; CAS(4,5) setup). We considered five quintet excited states, 35 triplet excited states, and 22 singlet excited states in our calculations. Zero-field splittings were then extracted using the effective Hamiltonian approach as implemented in the ORCA program. In the notation used to specify particular species, **1-π-^{3}TS1**, for example, denotes TS1 corresponding to species **1** in the triplet surface for the π reaction channel.

Results

Electronic structures of species 1 and 2

To address issues (i) and (ii) raised above, we computed the electronic structures of species **1** and **2**. Calculations yielded $S=1$ as the ground state for **1**, with an Fe–O bond length of 1.659 Å (see Figure 1a and Table S1 in the Supporting Informa-

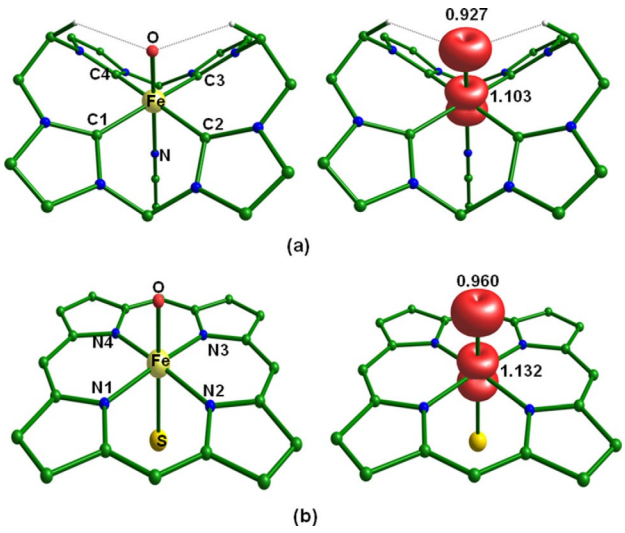

Figure 1. (a) B3LYP-D2-optimized structure of the ground state of $[(L^{NHC})Fe^{IV}(O)(MeCN)]^{2+}$ (**1**) and its corresponding spin density plot. (b) B3LYP-D2-optimized structure of the ground state of [(porphyrin)-$Fe^{IV}O(SH)]^{-}$ (**2**) and its corresponding spin density plot.

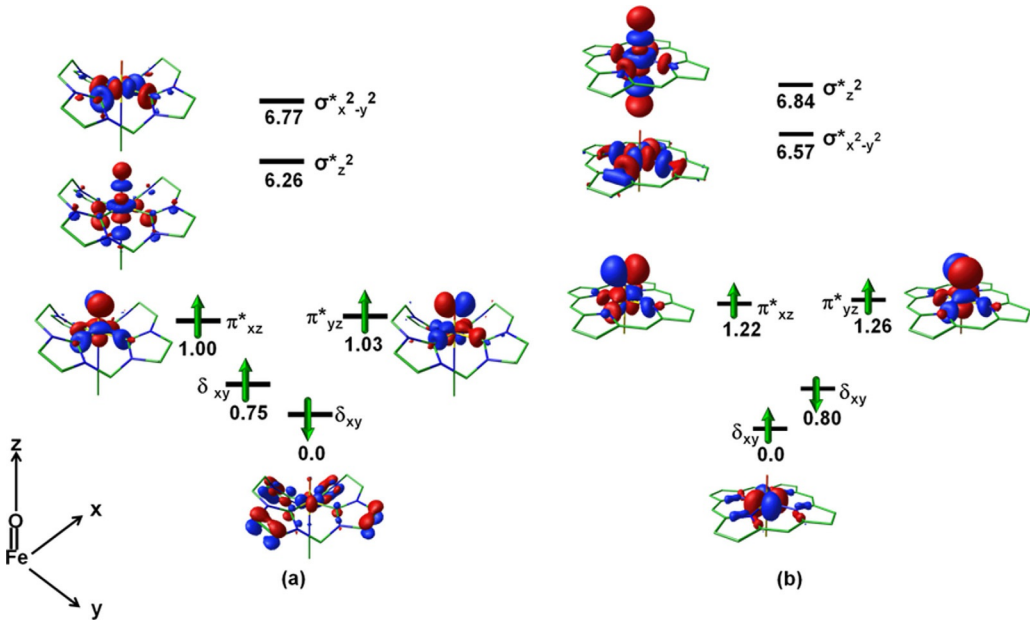

Figure 2. Eigenvalue plots for the ground states ($S=1$) of (a) **1** and (b) **2** (all values in eV).

tion). This and other structural parameters were in accordance with the reported X-ray structure.[10] The Fe–C distances were estimated as 1.986 and 2.043 Å, shorter than the equatorial Fe–N distances computed for **2**, thus reflecting stronger bonds. The electronic configuration for the ground state ($S=1$) of **1** was computed as $(\delta_{xy})^2(\pi^*_{xz})^1(\pi^*_{yz})^1(\sigma^*_{z^2})^0(\sigma^*_{x^2-y^2})^0$ (see Figure 2a), implying strong π overlap between the O $p_{x/y}$ orbitals and Fe d_{xz}/Fe d_{yz} orbitals. Besides, as the carbene ligands are nonplanar, their σ bonding orbitals are found to have bonding interactions with the π^*_{xz} and π^*_{yz} orbitals, leading to a reduction in the gap between the δ_{xy} and $\pi^*_{xz/yz}$ levels (0.25 eV, see Figure 2a). Unlike in conventional iron(IV)-oxo species, very strong equatorial ligation by the tetracarbene significantly destabilizes the $\sigma^*_{x^2-y^2}$ orbital in **1**.

To a certain extent, this also destabilizes the $\sigma^*_{z^2}$ orbital. Lower $\sigma^*_{z^2}$ energy also implies that the Fe–C equatorial ligand field is much stronger than the axial Fe–O and Fe–N bonds. As both of these orbitals are destabilized, there is a large energy penalty for attaining the $S=2$ high-spin state, placing it at 93.1 kJ mol^{-1} higher in energy compared to the $S=1$ state. This large energy gap (one of the largest energy gaps known) reduces the reactivity and contributes to the stability of species **1**.[10] Moreover, the optimized structure shows that each ethylene unit forms a weak C–H···O interaction with the ferryl oxygen atom, and this imparts **1** with additional stability (see Figure 1a). This stabilization can be compared to that imparted to a tripodal iron(IV)-oxo complex by three N–H···O hydrogen-bonding interactions.[21] To quantitatively assess the strength of this interaction, we performed NBO second-order perturbation theory donor–acceptor analysis, which placed this interaction energy at as high as 8 kJ mol^{-1}. Spin density at the iron centre for the ground state of **1** was computed as 1.103 (see Figure 1a). A significant spin density was also computed at the ferryl oxygen atom (0.927) in **1**, suggesting oxyl radical character (see Table S2 in the Supporting Information).[2a] The spin density on the oxygen atom of **2** was estimated as 0.960, slightly larger than that for **1** (see Figure 1b).

The electronic configuration for the quintet state of **1** is $(\delta_{xy})^1(\pi^*_{xz})^1(\pi^*_{yz})^1(\sigma^*_{z^2})^1(\sigma^*_{x^2-y^2})^0$. The Fe–O distance was estimated as 1.755 Å, and the Fe–N bond length to the acetonitrile ligand as 3.899 Å, leading to a distorted square-pyramidal geometry. The Fe–O distance found for the $S=2$ state is much longer than that for the $S=1$ state. This may be attributed to the presence of an unpaired electron in the antibonding $\sigma^*_{z^2}$ orbital, which reduces the Fe–O bond order. The elongation of the Fe–N bond in the $S=2$ state is due to strong pseudo-Jahn–Teller distortion, which favours elongation along the *z*-direction and compression along the Fe–C bond in **1**. A search for a second pseudo-Jahn–Teller isomer with longer Fe–C bonds and shorter axial bonds revealed no defined second minimum (the other isomer was found to lie around 27.2 kJ mol^{-1} higher in energy; see Figure S11 in the Supporting Information for a relaxed scan profile). Usually, non-heme complexes in the $S=2$ state possess an unpaired electron in the $\sigma^*_{x^2-y^2}$ orbital, giving rise to compression along the *z*-direction. Here, strong equatorial ligation and weak axial ligation of MeCN pushes the $\sigma^*_{x^2-y^2}$ orbital very high in energy, leading to a different electronic state (see Figure 3).

Although there is a reduction in the radical character at the ferryl oxygen atom of **1**, significant spin density is still detected at this atom, which suggests a possible C–H bond activation for this species. To fully comprehend the implications of the electronic structure, we computed the spectral features of **1**.

Calculations yielded a Mössbauer isomer shift δ of −0.139 mm s^{-1} and a quadrupole splitting parameter ΔE_Q of 2.97 mm s^{-1} for the $S=1$ state. The computed δ value is smaller than those reported for other iron(IV)-oxo species (in the range 0.15–0.20 mm s^{-1}).[10] The lower isomer shift for **1** reflects

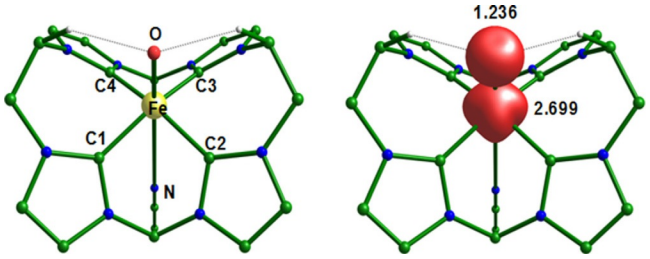

Figure 3. B3LYP-D2-optimized structure of the quintet state ($S=2$) of $[(L^{NHC})Fe^{IV}(O)(MeCN)]^{2+}$ (**1**) and its corresponding spin density plot.

the presence of the strong equatorial σ-donor macrocyclic tetracarbene ligand, which donates charge into the 4s orbital of the iron centre, as supported by NBO calculations. This charge transfer also enhances the stability of the iron(IV)-oxo species. The zero-field splitting parameter of the $S=1$ state has been estimated by the NEVPT2 approach[13,22] as $D=16.52$ cm^{-1} with $E/D=0.015$ cm^{-1}, in excellent agreement with earlier reports[10,23] (see Table 1). The estimated axial parameter D is smaller than those for other iron(IV)-oxo triplet states, suggesting a reduction in the spin-orbit coupling for **1**. A very large ZFS parameter generally suggests strong mixing of the spin states, a desired condition to observe two-state reactivity. Since the magnitude of the D parameter is small for **1**, this is likely to further affect its reactivity.[24]

Table 1. Computed spectroscopic parameters for **1**.

Fe^{IV}=O	ΔE_Q	δ [mm s^{-1}]	D [cm^{-1}]	E/D
$S=2$	−1.78	−0.117	–	–
$S=1$	2.97	−0.139	16.52	0.015
$S=0$	–	–	–	–
exp.[10]	3.08	−0.13	16.40	–

To compare the electronic structure and reactivity of **1** to those of a heme iron(IV)-oxo species, we chose to study [(porphyrin)Fe^{IV}(O)(SH)]$^-$ (**2**; see Figure 1 b). This is the active site structure of compound II (Cpd II) in cytochrome P450,[25] which has been shown to exhibit moderate reactivity compared to compound I of cytochrome P450. Besides, this particular model complex has also been prepared and its catalytic abilities towards C–H bond activation and the epoxidation of olefins have been tested.[2d,f] Similar to Cpd I of cytochrome P450, this species has also been found to feature a strong axial ligand effect on the reactivity. Our calculations reveal the ground state of **2** to be a triplet, with the $S=2$ level found to lie 38.7 kJ mol^{-1} higher in energy (see Table 2).[26] The electronic configuration for the ground state ($S=1$) of this species is computed to be $(\delta_{xy})^2(\pi^*_{xz})^1(\pi^*_{yz})^1(\sigma^*_{x^2-y^2})^0(\sigma^*_{z^2})^0$ (see Figure 2 b). Unlike in **1**, the $\pi^*_{xz/yz}$ orbitals are pure Fe–O orbitals, and the $\delta_{xy}-\pi^*_{xz/yz}$ gap is estimated to be 0.42 eV, much larger than that computed for **1**.

Reactivities of species 1 and 2 towards the hydroxylation of methane

To probe the reactivities of species **1** and **2**, we performed a computational study on methane activation.[27] This was specifically chosen as methane is known to be a very inert substrate (Scheme 2). Although the reactivity of **1** was unknown at the time of writing, very recently Mayer's group established the reactivity of **1** towards various substrates with relatively weaker C–H bonds, such as 1,4-cyclohexadiene, 9,10-dihydroanthracene, 9*H*-xanthene, and 9*H*-fluorene.[28] Besides, the reactivity of an Fe^{IV}=O carbene species with a slightly different architecture has been documented, and its C–H bond activation and oxygen-atom-transfer abilities have been demonstrated.[29]

The hydroxylation of methane is expected to proceed through a C–H bond activation step (via TS1) followed by the formation of a radical intermediate. Rebound of the -OH group from the intermediate to the radical species via TS2 leads to

Table 2. B3LYP-D2-computed relative energies (kJ mol^{-1}) of **1**, **1a**–**1d**, **2**, and **2a**. The potential-energy surface figures corresponding to the energies given here are shown in Figures S1–S5 and S9 in the Supporting Information.

Species	1	1a	1b	1c	1d	2	2a
^{5}**R**	93.1	97.6	78.6	86.2	50.6	38.7	49.2
^{3}**R**	0.0	0.0	0.0	0.0	0.0	0.0	0.0
^{1}**R**	121.1	129.0	124.3	120.9	111.6	123.0	133.4
σ-^{5}**TS1**	221.9	223.4	152.5	240.6	189.5	137.1	–
π-^{5}**TS1**	197.1	189.5	129.6	152.8	121.3	156.7	144.9
σ-^{3}**TS1**	183.2	141.0	71.2	165.0	107.1	–	–
π-^{3}**TS1**	123.2	128.3	120.5	118.0	138.0	110.7	125.5
^{1}**TS1**	238.1	258.4	236.9	231.9	259.0	226.3	–
^{7}**Int**	158.9	259.1	105.1	142.9	124.6	72.3	56.9
^{5}**Int**	84.0	114.7	101.4	69.3	97.2	90.5	139.8
^{3}**Int**	77.2	81.8	71.8	68.6	50.4	56.4	71.9
π-^{5}**TS2**	191.1	221.1	–		151.8	177.0	–
σ-^{3}**TS2**	138.7	156.2	184.0	128.6	138.6	132.9	131.4
^{1}**TS2**	208.3	202.8	–	–	265.9	167.4	–
^{5}**P**	14.3	40.2	−51.1	−11.0	−11.1	−91.4	−48.4
^{3}**P**	−41.7	−11.5	−110.1	−50.1	−77.2	−69.2	−72.6
^{1}**P**	−42.4	4.2	−42.2	−50.9	−8.6	−39.6	−57.3

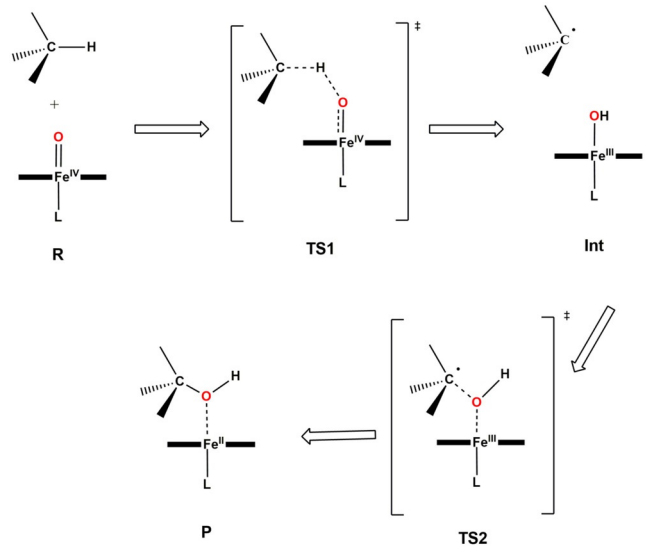

Scheme 2. Schematic depiction of the mechanism proposed for C–H bond activation of methane by iron(IV)-oxo species.

the hydroxylated product. For the C–H bond activation step, two different pathways, σ and π, based on the Fe–O–H angles are proposed.[30] In the σ pathway, an electron from the σ* orbital of the C–H bond is expected to occupy the $\sigma^*_{z^2}$ orbital of the metal. In the case of the π pathway, an electron from the C–H bond is expected to occupy the π^*_{xz}/π^*_{yz} orbitals of the metal. This is shown in the orbital evolution diagram in Figure 4. In the σ pathway (via **σ-TS1**), the Fe–O–H angle is expected to be close to 180°, whereas in the π pathway (via **π-TS1**), it should be close to 120°.[30]

The computed potential-energy surface for the hydroxylation of **1** is shown in Figure 5. For **1**, we computed five different C–H bond activation barrier heights for the $S=1$, 0, and 2 surfaces. The barrier height along the **1-π-^{3}TS1** channel is 123.2 kJ mol^{-1}, which is estimated to be the lowest, and for the **1-σ-^{3}TS1**, **1-π-^{5}TS1**, and **1-σ-^{5}TS1** channels, the barriers are estimated to be 183.2, 197.1, and 221.9 kJ mol^{-1}, respectively. For the $S=0$ singlet surface (**1-^{1}TS1**), a much higher barrier of 238.1 kJ mol^{-1} was obtained, and this ruled out the possibility of $S=0$ participating in this reaction. The lengths of the newly forming O–H bond at TS1 were found to be shorter for the triplet states (1.148 Å/1.108 Å for **1-σ-^{3}TS1**/**1-π-^{3}TS1**) than for the quintet states (1.168 Å/1.204 Å for **1-σ-^{5}TS1**/**1-π-^{5}TS1**; see Table S1 in the Supporting Information). The computed Fe–O–H angle for the lowest triplet transition state (**1-π-^{3}TS1**) is 114.8°, which corresponds to the π pathway (see Figure 6a). For the $S=2$ pathway, the Fe–O–H angle is estimated to be 110.0°, also suggesting a π pathway (**1-π-^{5}TS1**).

Generally, the $S=2$ state reacts via a σ pathway, as this maximizes the exchange energy leading to stabilization of the transition state and the observation of two-state reactivity (TSR). To further probe the reactivity of **1**, we also explored other reaction channels, for which we computed the σ pathways for the $S=1$ (**1-σ-^{3}TS1**) and $S=2$ states (**1-σ-^{5}TS1**) (see Figure 6b). These computed transition states were found to be even higher in energy at 183.2 and 221.9 kJ mol^{-1} (60.0 and

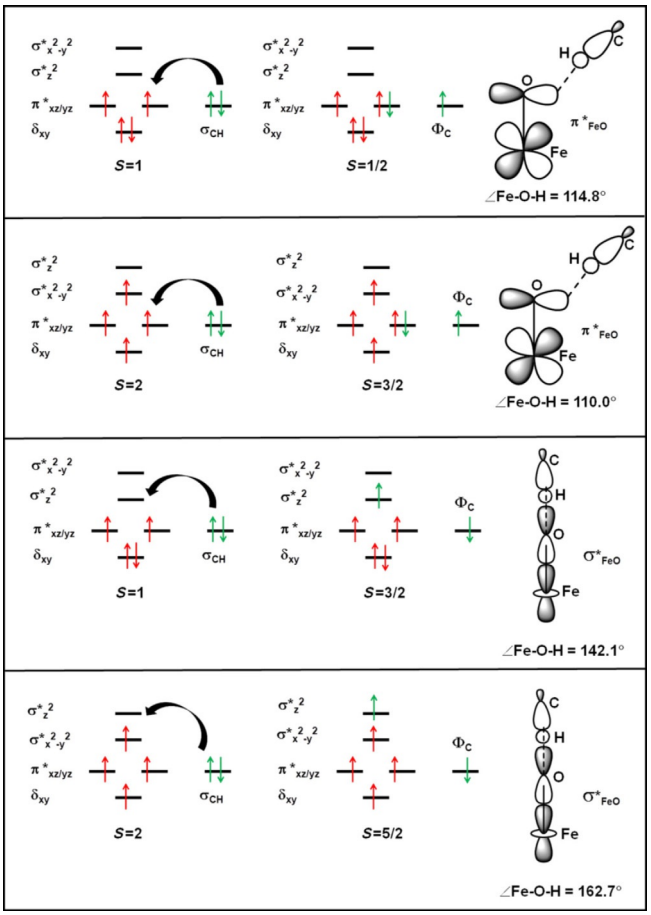

Figure 4. Orbital occupancy diagrams for the H-abstraction processes and corresponding orbital selection rules for predicting transition-state structures in **1**. The indicated Fe–O–H angles were obtained from the calculated results.

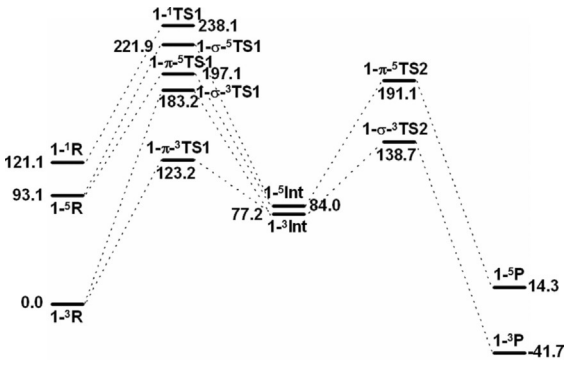

Figure 5. B3LYP-D2-computed potential-energy surface (ΔG in kJ mol^{-1}) for methane hydroxylation by $[(L^{NHC})Fe^{IV}(O)(MeCN)]^{2+}$ (**1**).

24.8 kJ mol^{-1} higher than the corresponding π pathways). This clearly suggests that the expected lowering of the kinetic barrier due to the choice of various reaction channels is absent in **1**, leading to the observation of a pure triplet-state reactivity.

In all of the computed **TS1** structures, clearly significant spin densities are detected at the carbon atom of the methane molecule (see Figure 7 and Table S2 in the Supporting Information). This suggests that the reaction proceeds via a radical

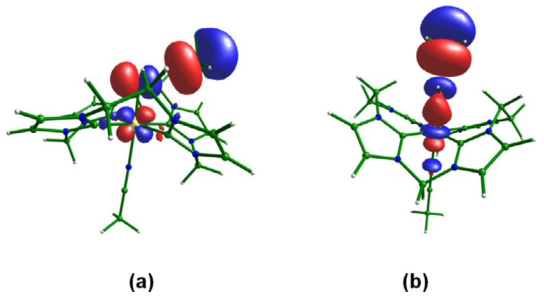

Figure 6. HOMOs of transition states for (a) **1-π-^{3}TS1** exhibiting π-interaction with the C–H bond, and (b) **1-σ-^{5}TS1** exhibiting σ-interaction.

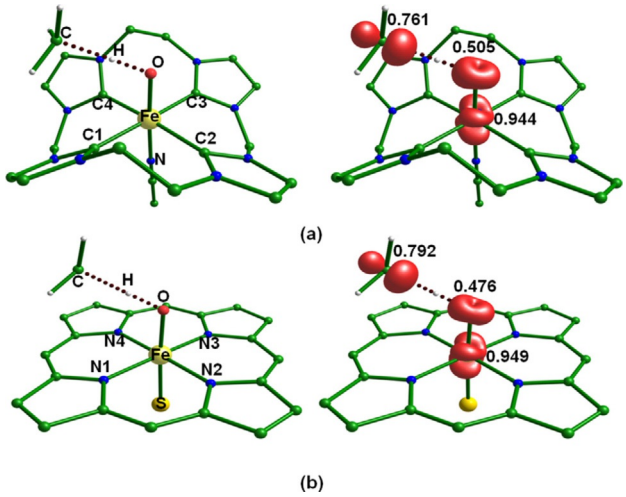

Figure 7. (a) B3LYP-D2-optimized structure of the lowest transition state for C–H bond activation by $[(L^{NHC})Fe^{IV}(O)(MeCN)]^{2+}$ (**1**) (**1-π-^{3}TS2**) and its corresponding spin density plot. (b) B3LYP-D2-optimized structure of the lowest transition state for C–H bond activation by $[(porphyrin)Fe^{IV}O(SH)]^-$ (**2**) (**2-π-^{3}TS2**) and its corresponding spin density plot.

pathway, as shown in Scheme 2. Hydrogen atom abstraction generates the Fe^{III}–OH intermediate. For this intermediate (**1-Int**), a triplet state is found to be the ground state, with the quintet state lying 6.8 kJ mol^{-1} higher in energy. Thermodynamically, formation of this intermediate (Fe^{III}–OH) is found to be endothermic by 77.2 kJ mol^{-1}. In the next step, -OH rebound is expected to occur. In some cases, the -OH rebound step has been computed to be rate-determining,[26] and therefore the estimation of this step becomes important to fully understand the reactivity pattern.

For species **1**, rebound barriers are estimated to be 138.7 kJ mol^{-1} on the triplet surface and 191.1 kJ mol^{-1} on the quintet surface. We also estimated the barrier height on the singlet surface and found it to be very high (208.3 kJ mol^{-1}; see Table 2).

Previously, Neese and co-workers[30a] reported that the reactivity of an Fe^{IV}=O group can be expected to follow a σ pathway for the H-abstraction followed by a π pathway for the rebound step, or vice versa. For the rebound at the **1-σ-^{3}TS2** transition state, the Fe–O–C bond angle is computed to be 157.7°, suggesting a σ-pathway (see Figure 8 and Table S1 in the Supporting Information).[26,31] Thus, the reaction follows a π

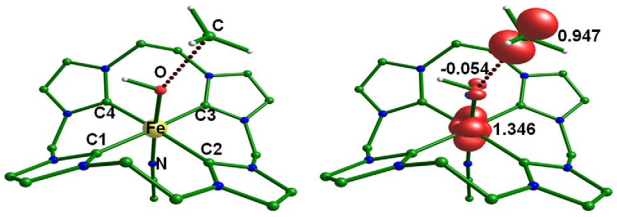

Figure 8. (a) B3LYP-D2-optimized structure of the lowest transition state of the OH rebound of $[(L^{NHC})Fe^{IV}(O)(CH_3CN)]^{2+}$ (**1**) (**1-σ-^{3}TS2**) and its corresponding spin density plot.

pathway for **TS1** followed by a σ pathway for the hydroxylation step. The very large barrier computed for the rebound step suggests that both the C–H bond activation and -OH rebound steps are associated with decisive kinetic barriers. The quintet state barriers were also estimated to be very high in energy, ruling out the possibility of the $S=2$ state participating in the reaction. Thus, the whole reaction is expected to occur along the triplet surface, following single-state reactivity. The final hydroxylation product is found to possess a triplet ground state and its formation is exothermic by 41.7 kJ mol^{-1}. Again, as both the reactant and the products possess the same spin multiplicity, a TSR scenario can be ruled out.

To compare the reactivities of **1** and **2**, we also computed the corresponding C–H bond activation transition states (see Figure 7 b). For **2**, the barrier heights are estimated as 110.7, 137.1, 156.7, and 226.3 kJ mol^{-1} for **2-π-^{3}TS1**, **2-σ-^{5}TS1**, **2-π-^{5}TS1**, and **2-^{1}TS1**, respectively (see Table 2 and Figure S1 in the Supporting Information). Also for **2**, the difference in barrier heights is larger, suggesting a possible triplet-state reactivity in the initial step, as has been evidenced in previous work.[26] The formation of the radical intermediate is found to be endothermic (56.4 kJ mol^{-1} on the triplet surface), and the rebound steps are estimated to have associated barrier heights of 132.9, 177.0, and 167.4 kJ mol^{-1} for transition states **2-σ-^{3}TS2**, **2-π-^{5}TS2**, and **2-σ-^{1}TS2**, respectively. Although the reaction is likely to proceed on the triplet surface until the rebound surface, the final hydroxylation product has a quintet ground state and its formation is exothermic by 91.7 kJ mol^{-1}. Since the final product has different multiplicity compared to the reactant, this suggests a possible spin crossover prior to formation of the product and invokes a likely TSR scenario for this reaction.

Role of axial ligands in the electronic structures and reactivities of 1 and 2

To assess the role of axial ligands in fine-tuning the reactivity, a series of complexes bearing thiol (-SH, **1 a**), tertiary amine ($N(CH_3)_3$, **1 b**), or tertiary phosphine ligands ($P(CH_3)_3$, **1 c**) or no ligand (**1 d**) at the axial position of **1** was modelled. Although such axial ligands have been routinely used in non-heme iron(IV)-oxo chemistry, variation of the axial ligands for **1** has not yet been tested experimentally. Additionally, we also modelled **2** with axial acetonitrile coordination (**2 a**) to compare and contrast the results with those for heme models. Our computed results show that, irrespective of the nature of the axial

ligation, the ground state is a triplet in all cases. The gaps between the triplet and quintet states are estimated to be 93.1, 97.6, 78.6, 86.2, 50.6, 38.7, and 49.2 kJ mol^{-1} for **1**, **1a**, **1b**, **1c**, **1d**, **2**, and **2a**, respectively (see Table 2). Clearly, the energies of the quintet states are very high-lying for all of the axial ligands tested for **1**, with the exception of **1d**, whereas for **2** only moderate gaps are detected, even with acetonitrile in the axial position.

The $S=1$ states of **1a**–**1d** have the electronic configuration $(\delta_{xy})^2(\pi^*_{xz})^1(\pi^*_{yz})^1(\sigma^*_{z^2})^0(\sigma^*_{x^2-y^2})^0$, as established for **1**. Among the axial ligands tested, the thiol group has the strongest electron-donating ability (basicity), followed by tertiary phosphine, tertiary amine, and acetonitrile. This is reflected in the Fe–O bond lengths, with the -SH group giving the longest such bonds with both carbene and porphyrin ligand moieties. Fe–O bond lengths decrease with $P(CH_3)_3$, $N(CH_3)_3$, CH_3CN, and no axial ligand (see Table S1 in the Supporting Information).[5d] The spin density at the oxygen centre is most informative with regard to the electrophilic/nucleophilic nature of the metal-oxygen bonds. All six species studied here have oxyl radical character at the ferryl oxygen centre, suggesting that they should behave as electrophiles. The strongest oxyl radical character was detected for species **2a**, followed by **2**. Among the various NHC-based species, the highest spin density was detected for **1**, and the lowest for **1d**. Interestingly, with both the porphyrin and the NHC moiety, an acetonitrile ligand was found to promote strong radical character.

The $S=2$ states of species **1a**–**1c**, on the other hand, have the electronic configuration $(\delta_{xy})^1(\pi^*_{xz})^1(\pi^*_{yz})^1(\sigma^*_{x^2-y^2})^1(\sigma^*_{z^2})^0$, with the $\sigma^*_{z^2}$ orbital being strongly destabilized with respect to $\sigma^*_{x^2-y^2}$ ($\Delta E(\sigma^*_{x^2-y^2}-\sigma^*_{z^2})\approx 2.7$ eV in all three cases). This is similar to the situation for the $S=2$ state of **2**, but contrary to those for **1** and **1d**. Due to this electronic configuration, the Fe–O bond lengths in **1a**–**1c** are barely altered compared to that for the triplet state (in the range 1.658–1.683 Å). However, the Fe–C bonds in these species are found to be longer (Fe–C_{avg} 2.004 and 2.152 Å for **1** and **1a**, respectively) compared to those in the $S=2$ state of **1** (see Table S1 in the Supporting Information). This suggests stabilization of a pseudo-Jahn–Teller compression along the Fe=O direction for the $S=2$ species. Stronger axial donation in **1a**–**1c** compared to MeCN/no axial ligand in **1** and **1d** stabilizes pseudo-Jahn–Teller compressed geometries for the former.

To further understand the influence of axial ligands on the reactivity, we also computed the C–H bond activation of methane by species **1a**–**1d** and **2a**. For species **1a**, the barrier heights are estimated as 128.3, 189.5, and 258.4 kJ mol^{-1} for the triplet, quintet, and singlet spin surfaces, respectively. Despite the presence of a strongly basic ligand in the axial position, the barrier heights are barely altered in **1a** compared to **1**, and the quintet state still lies very high in energy. The Fe–O–H bond angles for **1a**-^{3}**TS1** and **1a**-^{5}**TS1** are 113.3° and 110.2°, respectively, and this suggests a π pathway for the C–H bond activation on both the surfaces.[30a] To rule out the possibility that the σ pathway for $S=1$ and $S=2$ could be lower for **1a**, we also computed the corresponding transition states, **1a**-σ-^{3}**TS1** and **1a**-σ-^{5}**TS1**; these are estimated to lie 12.7 kJ mol^{-1} and 33.9 kJ mol^{-1} higher in energy compared to **1a**-π-^{3}**TS1** and **1a**-π-^{5}**TS1**, respectively (see Table 2 and Figure S2 in the Supporting Information). The Fe–O–H angle for the $S=2$ σ pathway is estimated to be 124.9°, far from linearity, suggesting weaker overlap and hence a larger kinetic barrier along this channel. To estimate the energy penalty required to form a linear Fe–O–H bond, we performed a single-point energy calculation on **1a**-σ-^{5}**TS1** by fixing the Fe–O–H angle at 180°. This geometry is found to lie 10.7 kJ mol^{-1} higher in energy compared to the ground state of **1a**-σ-^{5}**TS1**, and our attempt to obtain another transition state with a linear angle was unsuccessful. It is interesting to note here that, despite species **1a** having a different electronic configuration compared to species **1**, the estimated kinetics is very similar. Close scrutiny of the electronic structure of **1a**-π-^{5}**TS1** reveals that the unpaired electron resides in the $\sigma^*_{z^2}$ orbital and not the lower-lying $\sigma^*_{x^2-y^2}$ orbital found in the reactant state. This suggests that during the course of the reaction, the computed pseudo-Jahn–Teller compressed $S=2$ state switches to a pseudo-Jahn–Teller elongated state, resulting in a reactivity similar to that observed for **1**. To further verify this, the Fe–O bond lengths for the quintet state of the reactant and transition states **1**/**1a**-π-^{5}**TS1** are compared. For **1**, the Fe–O bond length is moderately elongated from 1.775 Å to 1.943 Å at transition state **1**-π-^{5}**TS1**, whereas in species **1a** the increase is more significant, from 1.683 Å to 2.041 Å (see Table S1 in the Supporting Information). As the ferryl oxygen atom accepts an H atom, the Fe=O π character is weakened, leading to a longer Fe–O bond at the transition state and hence a pseudo-Jahn–Teller elongated structure. MO analysis corroborates this picture, with $\sigma^*_{x^2-y^2}$ being vacant at the transition state. The longer Fe–O distance is accompanied by concomitantly shorter Fe–C distances in **1a**-π-^{5}**TS1** (Fe–C_{avg} 2.152 and 2.035 Å for the $S=2$ reactant and **1a**-π-^{5}**TS1**, respectively). Thus, despite the stronger donation by the -SH group, the reactivity pattern remains unaltered.

In the next step, H-atom abstraction generates an Fe^{III}–OH intermediate with an $S=1$ ground state, a process that is exothermic by 81.8 kJ mol^{-1}. For the rebound step, the triplet state (**1a**-^{3}**TS2**) is found to be lower in energy and here the Fe–O–C bond angle is computed as 147.6°, suggesting a σ pathway as seen for **1**. Formation of the hydroxylated product is exothermic (11.5 kJ mol^{-1}), and it possesses an $S=1$ ground state, obviating the need for spin-crossover on going from the reactant to the product.

We also explored the reactivities of species **1b**–**d** to further elucidate the overall reactivity pattern (see Table 2 and Figures S3–S5 in the Supporting Information). The computed geometries and electronic structures of species **1b** and **1c** are very similar to those of **1a** and thus are not elaborated further here (see Figures S6 and S7 in the Supporting Information). Likewise, the electronic structure of **1d** is similar to that of **1** (see Figure S8).

The C–H bond activation barriers for **1b**–**d** are estimated as 120.5, 118.0, and 138.0 kJ mol^{-1} for π-^{3}**TS1**, 71.2, 165.0, and 107.2 kJ mol^{-1} for σ-^{3}**TS1**, 129.6, 152.8, and 121.3 kJ mol^{-1} for π-^{5}**TS1**, and 152.5, 240.6, and 189.5 kJ mol^{-1} for σ-^{5}**TS1**, respectively (see Table 2 and Figures S3–S5 in the Supporting Infor-

mation). For all four species, the lowest-lying transition state is $S=1$, but there are some differences. Specifically, reactions with **1b** and **1d** are found to proceed via **σ-^{3}TS1**, that is, via a triplet σ channel, whereas in all other cases, the reactions are found to proceed through the triplet π pathway. Close inspection of the transition-state structure reveals that in **1b**, the axial $N(CH_3)_3$ group is cleaved and becomes weakly hydrogen-bonded to the NHC ligand (see Figure S8 in the Supporting Information). This is very similar to the transition-state structure computed for **1d**, which lacks an axial ligand. The reactivity of **1c** is found to be similar to that of **1a**. For **1d**, however, the **1d-π-^{5}TS1** transition state is only 14.2 kJ mol^{-1} higher in energy than the triplet transition state, suggesting a possible TSR scenario. A similar conclusion has also been reached for **1d** for other chemical transformations, such as epoxidation.[29] The energy differences between the lowest-lying $S=1$ and $S=2$ states are found to be very high for all of the species except **1d**, and this rules out the possibility of two-state reactivity for **1** and **1a–c**.

Formation of the radical intermediate (**Int**) is found to be endothermic for species **1b–1d** and for this intermediate $S=1$ is found to be the ground state in all three cases. The -OH rebound barriers are estimated to be 184.0, 128.6, and 138.6 kJ mol^{-1} for **1b-σ-^{3}TS2**, **1c-σ-^{3}TS2**, and **1d-σ-^{3}TS2**, respectively.[32] The products also have a triplet ground state and their formation is exothermic in all three cases (110.1, 50.1, and 77.2 kJ mol^{-1} for **1b**, **1c**, and **1d**, respectively). Besides, for species **2a**, the C–H bond activation step has barrier heights of 125.5 and 144.9 kJ mol^{-1} for **2a-π-^{3}TS1** and **2a-π-^{5}TS1**, respectively, here the lowest-lying transition state (**2a-π-^{3}TS1**) is higher than that observed for **2** (see Table 2 and Figure S9 in the Supporting Information). Formation of the intermediate is found to be endothermic in nature, and the rebound barrier computed on the triplet surface is estimated to be 131.4 kJ mol^{-1} (**2a-σ-^{3}TS2**), similar to that observed for **2**.

Discussion

TSR is a key concept in high-valent iron(IV)-oxo chemistry, and has been invoked as one of the reasons for the very high reactivity observed. Over the years, many factors influencing this reactivity have been explored, of which the donor ability of the axial ligand has been emphasized as the most important. This has been witnessed both experimentally and theoretically. However, in all of the cases tested, the equatorial ligands have been only moderate donors compared to the combined effect of an oxygen atom and the axial ligand. If this scenario is changed, as in the present case, this may dramatically influence the reactivity pattern.

The electronic structures of **1** and **2** differ drastically, both in the triplet ground states and in the important first excited quintet states. The most striking difference is in the energies of the σ* orbitals, with $\sigma^*_{z^2}$ being lower in energy for **1**, but $\sigma^*_{x^2-y^2}$ being lower in energy for **2**. Higher reactivity of an iron(IV)-oxo group stems from lower barrier height at the transition state for the quintet state. Generally, the quintet state reacts via a σ pathway, whereby it accepts an α electron in the $\sigma^*_{z^2}$ orbital. This maximizes the exchange energy and thereby stabilizes the transition state. For **2** and other non-heme iron(IV)-oxo species having an empty low-lying $\sigma^*_{z^2}$ orbital,[33] this scenario holds true, leading to higher reactivity.[34]

On the other hand, for **1**, as the $\sigma^*_{z^2}$ orbital is already filled, only the $\sigma^*_{x^2-y^2}$ orbital can accept an α electron in the σ pathway. As this orbital is strongly destabilized in **1**, this more than compensates for the additional exchange stabilization available along the σ $S=2$ pathway, leading to the lower unconventional π $S=2$ pathway. This precludes the possibility of $S=2$ participating in the reactivity of **1**. The absence of TSR is clearly visible beyond the first transition state, with the $S=1$ state for the intermediate being stabilized, a significantly lower barrier for the triplet state associated with the rebound step, and formation of an Fe^{II} product having an unusual $S=1$ state. Thus, the entire reaction proceeds on a triplet surface, leading to single-state reactivity. For **2**, the barrier heights computed for the triplet and quintet states are closer, but not close enough to suggest a TSR scenario. However, the Fe^{II} product has an $S=2$ quintet ground state, suggesting a spin crossover after the rebound step, and raising the possibility of TSR. Previous theoretical studies on this species for other chemical transformations support this interpretation.[28,29]

Although axial ligands are found to influence the reactivities of several heme and non-heme iron(IV)-oxo complexes, the reactivity pattern computed for **1a–c** is very similar to that computed for **1**. Clearly, the axial ligand modulates the electronic configuration of the $S=2$ state, with a very strong donor destabilizing the $\sigma^*_{z^2}$ orbital (see Figure 9, top). However, triplet-state orbital ordering and reactivity patterns are unaltered across the series (see Figure 8, bottom). An axial ligand would be expected to particularly influence the $\pi^*_{xz/yz}$ orbital, but here we have not witnessed any noticeable changes in the orbital splitting/ordering. This is perhaps due to the π-acceptor property of the carbene, which may compensate for any effect exerted by the axial ligands (see Figure 9, bottom, and Figure S10 in the Supporting Information). Moreover, the nature of the $S=2$ state is found to switch from one pseudo-Jahn–Teller isomer to another during formation of the transition state (TS1). For this reason, the σ $S=2$ pathway is found to be higher in energy compared to the unconventional π $S=2$ pathway for these species (with the exception of **1b**). As seen for **1**, occupation of the $\sigma^*_{x^2-y^2}$ orbital is required along the σ $S=2$ pathway, and this is unlikely to be influenced by the nature of the axial ligand. This again dictates very similar reactivity across the series studied. For **1d**, which lacks axial ligands, calculations lead to a different picture, in which the σ $S=1$ and π $S=2$ transition states are energetically similar in the rate-determining C–H bond activation step. This unequivocally suggests TSR for this species, as has also been witnessed for other tested reactions.[29]

To compare and contrast the reactivities among all of the species computed, we have plotted all of the lowest-energy pathways obtained for **1**, **1a–d**, **2**, and **2a** in Figure 10. Clearly, the barrier heights computed on the π $S=1$ surface for **1** and **1a–c** are unaltered, and the $S=2$ σ pathway is high-lying. For **2** and **2a**, a larger difference in the barrier heights is noted,

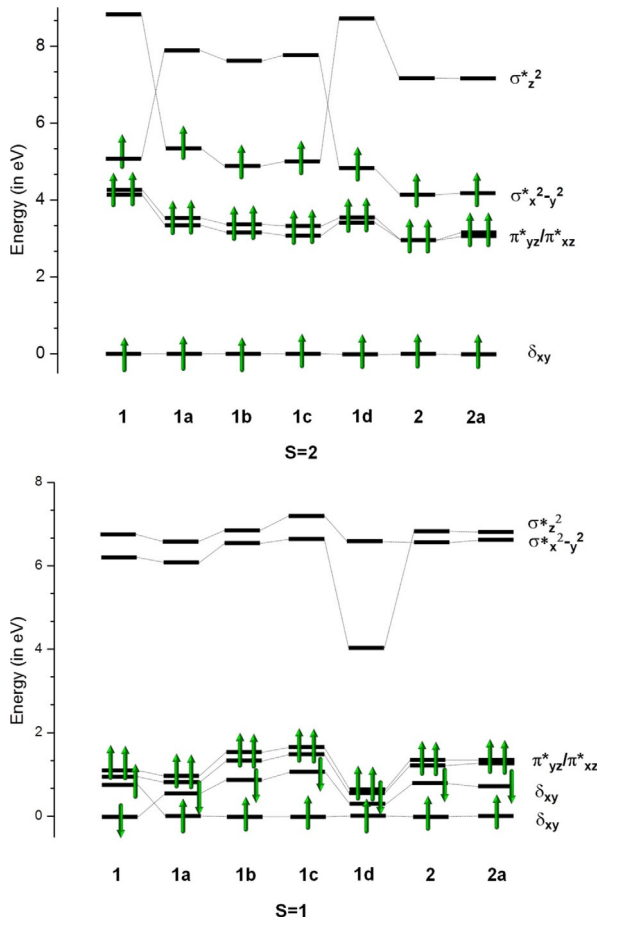

Figure 9. Orbital energy diagram for **1**, **1a**–**1d**, **2**, and **2a** in their triplet and quintet states.

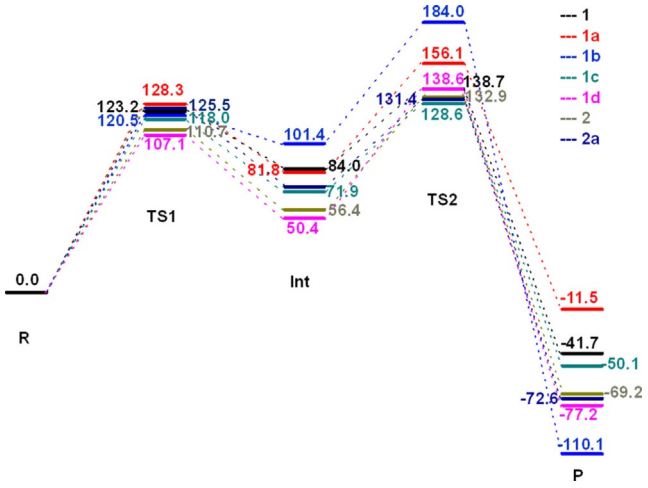

Figure 10. B3LYP-D2-computed potential-energy surfaces (ΔG in kJ mol^{-1}) for comparison of the triplet-state reactivities of **1**, **1a**, **1b**, **1c**, **1d**, **2**, and **2a**.

but closer margins and multiplicities of the product suggest a TSR scenario. Significant barrier heights are also noted for the rebound step for each of the species, suggesting that both steps are important in determining the kinetics of the reaction. For **1**, **1a**, **1c**, and **1d**, the reaction is found to proceed via a π $S=1$ path in the C–H activation step, followed by a σ $S=1$ path in the rebound step, leading to an $S=1$ product. For **1b**, however, slight differences are noted, and the reaction is found to proceed via a σ $S=1$ path in the C–H bond activation step. For **2**, on the other hand, the reaction proceeds via a π $S=1$ followed by a σ $S=1$ pathway, leading to an $S=2$ product.

Conclusions

From the above calculations, it is clear that **1** does not exhibit two-state reactivity. This is essentially due to very strong equatorial donation pushing the $\sigma^*_{x^2-y^2}$ orbital to higher energy. Together with the already destabilized $\sigma^*_{z^2}$ orbital due to the strong Fe^{IV}=O bond, this ensures that the reaction proceeds only along the triplet surface. Axial tuning by altering the $\sigma^*_{z^2}$ orbital energy does not bring about larger transformations to make the quintet state accessible. This is clearly evident when both the σ and π pathways are calculated for the quintet/triplet states. Unlike the usual iron(IV)-oxo reactivity, where σ $S=2$ is low-lying in energy, here the $S=2$ state also prefers to react via a π pathway, leading to sluggish reactivity (except in the case of **1b**). Besides the C–H bond activation step, there is also a substantial barrier associated with the rebound step, and this further hinders the reactivity. Secondly, axial ligands are found to have very little effect on the reactivity, and the barrier heights computed on the σ triplet surface for various axial ligands are very similar, affirming the above statement.

In summary, comprehensive DFT calculations have been employed to probe the electronic structures and reactivities of iron(IV)-oxo species bearing strong equatorial carbene ligands. These species are found not to exhibit two-state reactivity as the quintet states are found to lie very high in energy and the axial ligands do not significantly influence their electronic structure/reactivity. Both of these points are contrary to established concepts in heme and non-heme iron(IV)-oxo chemistry, and stress the need to also focus on designing appropriate equatorial ligands for fine-tuning of the reactivity.

Acknowledgements

G.R. would like to acknowledge financial support from the Government of India through the Department of Science and Technology (EMR/2014/000247) and generous computational resources from the NPSF. A.A. would also like to acknowledge financial support from the DST-SERB (ECR/2016/001111). R.K. thanks the CSIR for a fellowship.

Conflict of interest

The authors declare no conflict of interest.

Keywords: carbene ligands · density functional calculations · equatorial ligation · iron(IV)-oxo · *N*-heterocyclic carbenes · two-state reactivity

[1] a) W. N. Oloo, L. Que, Jr., *Acc. Chem. Res.* **2015**, *48*, 2612 – 2621; b) C. Krebs, D. G. Fujimori, C. T. Walsh, J. M. Bollinger, Jr., *Acc. Chem. Res.* **2007**, *40*, 484 – 492; c) W. Nam, *Acc. Chem. Res.* **2007**, *40*, 522 – 531.

[2] a) S. Shaik, S. Cohen, Y. Wang, H. Chen, D. Kumar, W. Thiel, *Chem. Rev.* **2010**, *110*, 949 – 1017; b) P. R. O. de Montellano, *Chem. Rev.* **2010**, *110*, 932 – 948; c) S. Shaik, D. Kumar, S. P. de Visser, A. Altun, W. Thiel, *Chem. Rev.* **2005**, *105*, 2279 – 2328; d) S. Kozuch, T. Leifels, D. Meyer, L. Sbaragli, S. Shaik, W.-D. Woggon, *Synlett* **2005**, 675 – 684; e) B. Meunier, S. P. de Visser, S. Shaik, *Chem. Rev.* **2004**, *104*, 3947 – 3980; f) S. P. de Visser, F. Ogliaro, P. K. Sharma, S. Shaik, *J. Am. Chem. Soc.* **2002**, *124*, 11809 – 11826; g) W. Nam, Y. M. Goh, Y. J. Lee, M. H. Lim, C. Kim, *Inorg. Chem.* **1999**, *38*, 3238 – 3240; h) M. Sono, M. P. Roach, E. D. Coulter, J. H. Dawson, *Chem. Rev.* **1996**, *96*, 2841 – 2888; i) J. T. Groves, Z. Gross, M. K. Stern, *Inorg. Chem.* **1994**, *33*, 5065 – 5072; j) T. E. Nemo, B. Evans, *J. Am. Chem. Soc.* **1981**, *103*, 2884 – 2886.

[3] W. Nam, S.-E. Park, I. K. Lim, M. H. Lim, J. Hong, J. Kim, *J. Am. Chem. Soc.* **2003**, *125*, 14674 – 14675.

[4] a) D. F. Leto, A. A. Massie, D. B. Rice, T. A. Jackson, *J. Am. Chem. Soc.* **2016**, *138*, 15413 – 15424; b) D. Schröder, S. Shaik, H. Schwarz, *Acc. Chem. Res.* **2000**, *33*, 139 – 145; c) P. Comba, M. Kerscher, W. Schiek, in *Progrees in Inorganic Chemistry*, Wiley, Chichester, **2007**, pp. 613 – 704; d) W. Nam, Y.-M. Lee, S. Fukuzumi, *Acc. Chem. Res.* **2014**, *47*, 1146 – 1154.

[5] a) S. P. de Visser, L. Tahsini, W. Nam, *Chem. Eur. J.* **2009**, *15*, 5577 – 5587; b) S. P. de Visser, *J. Biol. Inorg. Chem.* **2006**, *11*, 168 – 178; c) T. Kamachi, T. Kouno, W. Nam, K. Yoshizawa, *J. Inorg. Biochem.* **2006**, *100*, 751 – 754.

[6] a) H. Hirao, L. Que, W. Nam, S. Shaik, *Chem. Eur. J.* **2008**, *14*, 1740 – 1756; b) C. V. Sastri, J. Lee, K. Oh, Y. J. Lee, J. Lee, T. A. Jackson, K. Ray, H. Hirao, W. Shin, J. A. Halfen, J. Kim, L. Que, S. Shaik, W. Nam, *Proc. Natl. Acad. Sci. USA* **2007**, *104*, 19181 – 19186; c) C. V. Sastri, M. J. Park, T. Ohta, T. A. Jackson, A. Stubna, M. S. Seo, J. Lee, J. Kim, T. Kitagawa, E. Münck, *J. Am. Chem. Soc.* **2005**, *127*, 12494 – 12495; d) T. A. Jackson, J.-U. Rohde, M. S. Seo, C. V. Sastri, R. DeHont, A. Stubna, T. Ohta, T. Kitagawa, E. Münck, W. Nam, *J. Am. Chem. Soc.* **2008**, *130*, 12394 – 12407.

[7] R. Zhong, A. C. Lindhorst, F. J. Groche, F. E. Kühn, *Chem. Rev.* **2017**, *117*, 1970 – 2058.

[8] D. A. Sharon, D. Mallick, B. Wang, S. Shaik, *J. Am. Chem. Soc.* **2016**, *138*, 9597 – 9610.

[9] a) S. A. Cramer, D. M. Jenkins, *J. Am. Chem. Soc.* **2011**, *133*, 19342 – 19345; b) F. E. Hahn, V. Langenhahn, T. Lügger, T. Pape, D. Le Van, *Angew. Chem. Int. Ed.* **2005**, *44*, 3759 – 3763; *Angew. Chem.* **2005**, *117*, 3825 – 3829.

[10] S. Meyer, I. Klawitter, S. Demeshko, E. Bill, F. Meyer, *Angew. Chem. Int. Ed.* **2013**, *52*, 901 – 905; *Angew. Chem.* **2013**, *125*, 935 – 939.

[11] a) S. P. de Visser, *Angew. Chem. Int. Ed.* **2006**, *45*, 1790 – 1793; *Angew. Chem.* **2006**, *118*, 1822 – 1825; b) S. J. Kim, R. Latifi, H. Y. Kang, W. Nam, S. P. de Visser, *Chem. Commun.* **2009**, 1562 – 1564; c) A. Ansari, A. Kaushik, G. Rajaraman, *J. Am. Chem. Soc.* **2013**, *135*, 4235 – 4249; d) A. Ansari, M. Ansari, A. Singha, G. Rajaraman, *Chem. Eur. J.* **2017**, *23*, 10110 – 10125; e) A. Ansari, G. Rajaraman, *Phys. Chem. Chem. Phys.* **2014**, *16*, 14601 – 14613; f) P. Jayapal, A. Ansari, G. Rajaraman, *Inorg. Chem.* **2015**, *54*, 11077 – 11082.

[12] Gaussian 09 (Revision 02), M. J. Frisch, G. W. Trucks, H. B. Schlegel, G. E. Scuseria, M. A. Robb, J. R. Cheeseman, G. Scalmani, V. Barone, B. Mennucci, G. A. Petersson, H. Nakatsuji, M. Caricato, X. Li, H. P. Hratchian, A. F. Izmaylov, J. Bloino, G. Zheng, J. L. Sonnenberg, M. Hada, M. Ehara, K. Toyota, R. Fukuda, J. Hasegawa, M. Ishida, T. Nakajima, Y. Honda, O. Kitao, H. Nakai, T. Vreven, J. A. Montgomery, Jr., J. E. Peralta, F. Ogliaro, M. Bearpark, J. J. Heyd, E. Brothers, K. N. Kudin, V. N. Staroverov, R. Kobayashi, J. Normand, K. Raghavachari, A. Rendell, J. C. Burant, S. S. Iyengar, J. Tomasi, M. Cossi, N. Rega, J. M. Millam, M. Klene, J. E. Knox, J. B. Cross, V. Bakken, C. Adamo, J. Jaramillo, R. Gomperts, R. E. Stratmann, O. Yazyev, A. J. Austin, R. Cammi, C. Pomelli, J. W. Ochterski, R. L. Martin, K. Morokuma, V. G. Zakrzewski, G. A. Voth, P. Salvador, J. J. Dannenberg, S. Dapprich, A. D. Daniels, Ö. Farkas, J. B. Foresman, J. V. Ortiz, J. Cioslowski, D. J. Fox, Gaussian, Inc., Wallingford, CT, **2009**.

[13] F. Neese, *WIRES* **2012**, *2*, 73 – 78.

[14] S. Grimme, *J. Comput. Chem.* **2006**, *27*, 1787 – 1799.

[15] a) R. Ditchfield, W. J. Hehre, J. A. Pople, *J. Chem. Phys.* **1971**, *54*, 724 – 728; b) P. J. Hay, W. R. Wadt, *J. Chem. Phys.* **1985**, *82*, 299 – 310.

[16] a) A. Schäfer, H. Horn, R. Ahlrichs, *J. Chem. Phys.* **1992**, *97*, 2571 – 2577; b) A. Schäfer, C. Huber, R. Ahlrichs, *J. Chem. Phys.* **1994**, *100*, 5829 – 5835; c) B. Pandey, A. Ansari, N. Vyas, G. Rajaraman, *J. Chem. Sci.* **2015**, *127*, 343 – 352; d) M. Jaccob, A. Ansari, B. Pandey, G. Rajaraman, *Dalton Trans.* **2013**, *42*, 16518 – 16526.

[17] G. Zhurko, D. Zhurko, *Lite Version Build* **2005**, *8*, 2005.

[18] J. Tomasi, B. Mennucci, R. Cammi, *Chem. Rev.* **2005**, *105*, 2999 – 3094.

[19] a) M. Radoul, M. Sundararajan, A. Potapov, C. Riplinger, F. Neese, D. Goldfarb, *Phys. Chem. Chem. Phys.* **2010**, *12*, 7276 – 7289; b) M. Römelt, S. Ye, F. Neese, *Inorg. Chem.* **2009**, *48*, 784.

[20] F. Neese, *J. Am. Chem. Soc.* **2006**, *128*, 10213 – 10222.

[21] C. E. MacBeth, R. Gupta, K. R. Mitchell-Koch, V. G. Young, G. H. Lushington, W. H. Thompson, M. P. Hendrich, A. Borovik, *J. Am. Chem. Soc.* **2004**, *126*, 2556 – 2567.

[22] S. F. Ye, F. Neese, *J. Chem. Theory Comput.* **2012**, *8*, 2344 – 2351.

[23] S. Ye, C. Kupper, S. Meyer, E. Andris, R. Navrátil, O. Krahe, B. Mondal, M. Atanasov, E. Bill, J. Roithová, F. Meyer, F. Neese, *J. Am. Chem. Soc.* **2016**, *138*, 14312 – 14325.

[24] a) J. N. Harvey, M. Aschi, H. Schwarz, W. Koch, *Theor. Chem. Acc.* **1998**, *99*, 95 – 99; b) H. Chen, W. Lai, S. Shaik, *J. Phys. Chem. B* **2011**, *115*, 1727 – 1742.

[25] a) K. L. Stone, L. M. Hoffart, R. K. Behan, C. Krebs, M. T. Green, *J. Am. Chem. Soc.* **2006**, *128*, 6147 – 6153; b) E. Derat, S. Shaik, *J. Am. Chem. Soc.* **2006**, *128*, 8185 – 8198.

[26] A. Rosa, G. Ricciardi, *Inorg. Chem.* **2012**, *51*, 9833 – 9845.

[27] M. Ansari, N. Vyas, A. Ansari, G. Rajaraman, *Dalton Trans.* **2015**, *44*, 15232 – 15243.

[28] C. Kupper, B. Mondal, J. Serrano-Plana, I. Klawitter, F. Neese, M. Costas, S. Ye, F. Meyer, *J. Am. Chem. Soc.* **2017**, *139*, 8939 – 8949.

[29] F. G. C. Reinhard, S. P. de Visser, *Chem. Eur. J.* **2017**, *23*, 2935 – 2944.

[30] a) S. Ye, F. Neese, *Proc. Natl. Acad. Sci. USA* **2011**, *108*, 1228 – 1233; b) B. Pandey, M. Jaccob, G. Rajaraman, *Chem. Commun.* **2017**, *53*, 3193 – 3196.

[31] G. Ricciardi, E. J. Baerends, A. Rosa, *ACS Catal.* **2016**, *6*, 568 – 579.

[32] L. Ji, A. Franke, M. Brindell, M. Oszajca, A. Zahl, R. van Eldik, *Chem. Eur. J.* **2014**, *20*, 14437 – 14450.

[33] S. N. Dhuri, M. S. Seo, Y. M. Lee, H. Hirao, Y. Wang, W. Nam, S. Shaik, *Angew. Chem. Int. Ed.* **2008**, *47*, 3356 – 3359; *Angew. Chem.* **2008**, *120*, 3404 – 3407.

[34] S. Hong, P. Kumar, K. B. Cho, Y. M. Lee, K. D. Karlin, W. Nam, *Angew. Chem. Int. Ed.* **2016**, *55*, 12403 – 12407; *Angew. Chem.* **2016**, *128*, 12591 – 12595.

Manuscript received: January 25, 2018

Accepted manuscript online: March 5, 2018

Version of record online: March 5, 2018